# Negatively Charged Magnetite Nanoparticle Clusters as Efficient MRI Probes for Dendritic Cell Labeling and In Vivo Tracking

*Changqiang Wu, Ye Xu, Li Yang, Jun Wu, Wencheng Zhu, Danyang Li, Zhuzhong Cheng, Chunchao Xia, Yingkun Guo, Qiyong Gong, Bin Song, and Hua Ai**

**Cell labeling and tracking via magnetic resonance imaging (MRI) has drawn much attention for its noninvasive property and longitudinal monitoring functionality. Employing of imaging probes with high labeling efficiency and good biocompatibility is one of the essential factors that determine the outcome of tracking. In this study, negatively charged superparamagnetic iron oxide (PAsp-PCL/SPIO) nanoclusters are developed for dendritic cell (DC) labeling and tracking in vivo. PAsp-PCL/SPIO has a diameter of 124 ± 41 nm in DLS, negatively charged surface (zeta potential = –27 mV), and presents high $T_2$ relaxivity (335.6 Fe mM$^{-1}$ s$^{-1}$) and good DC labeling efficiency. Labeled DCs are unaffected in their viability, proliferation, and differentiation capacity, and have an excellent MR imaging sensitivity in vitro. To monitor the migration of DCs into lymphoid tissues in vivo, which will be related to the final immunotherapy results, $T_2$-wighted and $T_2$-map imaging of popliteal nodes at different points in time are acquired under a clinical 3 T scanner after subcutaneous injection of a certain number of labeled DCs at hindleg footpads of mice. The signal intensities decreasing and $T_2$ values shortening of ipsilateral popliteal nodes are significant and display a time- and dose-dependence, showing DCs' migration to the draining lymph nodes.**

## 1. Introduction

Recently, labeling and tracking therapeutic cell in vivo via magnetic resonance imaging (MRI) has invoked great interest.[1] Especially, high-sensitivity contrast agents greatly expanded the detection ability of MR imaging, lending it a hopeful tool for clinically monitoring the microscopic activities of cells in human body. Over the past two decades, many MRI probes were proposed for such purposes. However, few are approved for clinical applications. Superparamagnetic iron oxide (SPIO) nanoparticles are perhaps the most preferred, because only micromolar concentration is enough to induce a detectable change of MR signal intensity (SI).[1e,2] Nowadays, dextran-coated SPIO nanoparticles,[3] Feridex and Resovist, have been clinically approved as $T_2$ contrast agents. Nevertheless, in spite of their good biocompatibility, both have shown insufficient intracellular uptake and relaxivity for cell tracking.[4]

For cell labeling, the surface coating of probes stands as a key determinant, as important as size and morphology, etc. Therefore, chemical modification of the surface represents a major strategy. To promote cellular uptake of probes, positively charged transfection agent mediated approaches have been used.[2c,5] Formed complexes tend to aggregate onto the negatively charged cellular membrane by electrostatic interaction, hence facilitating internalization. However, these agents showed obvious cytotoxicity to cells,[6] resulting in differentiation inhibition,[7] apoptosis, or even death. Furthermore, these probes tend to electrostatically adsorption on the surface of cells rather than internalization.[8]

In recent years, negatively charged materials coated SPIO nanoparticles have been considered a good alternative to the positive ones with better biosafety. Existing data, though limited, revealed that these probes also have good results in cellular uptake efficiency and $T_2$ relaxivity.[9] Although the mechanisms are not completely understood, it is reasonable to believe that anionic SPIO nanoparticles would partly cover the inherent flaws of their cationic counterparts, and at least be suitable for the labeling and tracking of phagocytes. In

Dr. C. Wu, Dr. Y. Xu, L. Yang, J. Wu, W. Zhu, D. Li, Z. Cheng, Prof. H. Ai
National Engineering Research Center for Biomaterials
Sichuan University
Chengdu 610064, China
E-mail: huaai@scu.edu.cn
Dr. Y. Xu, Prof. H. Ai
Department of Radiology
Children's Hospital
Chongqing Medical University
Chongqing 400014, China
C. Xia, Prof. Q. Gong, Prof. B. Song
Department of Radiology
West China Hospital
Sichuan University
Chengdu 610041, China
Dr. Y. Guo
Department of Medical Imaging
West China Second University Hospital
Sichuan University
Chengdu 610041, China

DOI: 10.1002/adfm.201501031

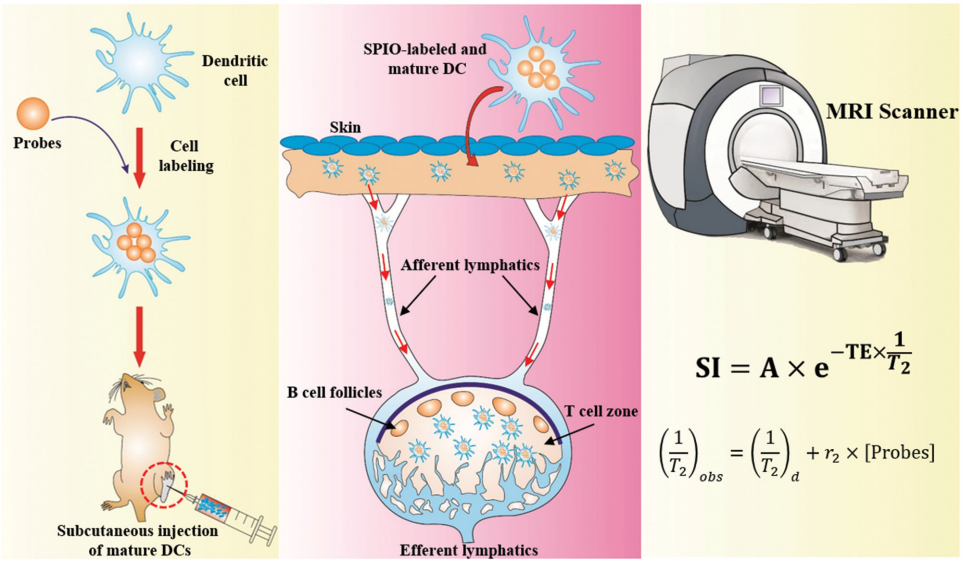


**Figure 1.** Dendritic cell labeling with magnetic nanoparticles and MRI tracking in vivo.

this study, we attempted to develop a biocompatible anionic MR imaging probe, composed with negatively charged block copolymer, poly(aspartic acid)-*b*-poly(ε-caprolactone) (PAsp-PCL). This amphiphilic block polymer is made up of nontoxic and biodegradable polymeric materials, widely used in clinic.[10] Herein, we utilized this MR imaging probe to label an important immunocyte, dendritic cell (DC), which is used for treating of different diseases clinically. Its migration in vivo was further monitored under a clinical 3.0 T MR imager (**Figure 1**). We chose DCs for the research based on the following reasons. First, DC, as an antigen-presenting cell, being particularly sensitive to exogenous stimulators, probes that bring little impact on DC are believed suitable to label inerter cells as well. Second, DCs are highly specialized antigen-presenting cells of the immune system and play a key role in immunotherapy. In recent years, DC-based anticancer immunotherapy was carried out in numerous clinical trials, and had a possible influence on clinical response.[11] So, the migration and immunization activities of DCs in vivo are needed to be timely monitored.

## 2. Results and Discussion

### 2.1. Preparation of PAsp-PCL/SPIO Nanocomposites

Block copolymer PAsp(OBzl)-PCL was synthesized through two-step ring opening polymerization of ε-caprolactone and Asp(OBzl)-NCA (Figure S1, Supporting Information). First, ring opening polymerization (ROP) of ε-caprolactone was initiated using 2-(carbobenzoxyamino)-1-ethanol to obtain the polymer Cbz-N-PCL. Carbobenzoxy was removed by high-pressure hydrogenation to obtain amino terminal PCL, a macroinitiator able to initiate ROP of Asp(OBzl)-NCA to obtain a diblock copolymer, PAsp(OBzl)-PCL. Then, benzyl groups on the side chains of this copolymer were removed to obtain amphiphilic diblock copolymer PAsp-PCL.[12] Number-average molecular weight of each block was estimated by the relative intensities in $^1$H NMR, and the end product was accordingly denoted as $PAsp_{50}$-$PCL_{65}$. Critical micelle concentration (CMC) of PAsp-PCL micelle was 0.821 mg $L^{-1}$, which was determined by the pyrene fluorescence methodology (Figure S5, Supporting Information). It demonstrated that the amphiphilic polymer PAsp-PCL can form stable micelle structures in an aqueous solution at lower concentrations.

Monodispersed SPIO nanoparticles were synthesized using the organic high temperature decomposition method,[13] and then transferred into aqueous phase with the help of amphiphilic polymer PAsp-PCL (**Figure 2**a) at a mass ratio of 3/1 (polymer/SPIO). The PAsp-PCL/SPIO nanocomposites showed excellent water solubility. Characterized by dynamic light scattering (DLS) (Figure 2b), the diameter of PAsp-PCL/SPIO nanocomposites (124 ± 41 nm) was obviously larger than simple organic SPIO nanocrystals (12 ± 3 nm), indicating that organic SPIO were successfully encapsulated in PAsp-PCL nanomicelles and formed into SPIO nanoclusters during phase transferring. Under scanning electronic microscopy (SEM) (Figure 2c), the nanocomposites appeared spherical in shape with particle sizes around 100 nm. Transmission electronic microscopy (TEM) (Figure 2d) image shows that SPIO nanocrystals are largely presenting as isolated clusters with dense packing. Subsequently, mean zeta potential was analyzed and resulted to be –27 mV. The negative charge was speculated to be derived from the carboxyl groups on the PAsp block at the surface of the nanoclusters. The formed PAsp-PCL/SPIO nanocomposites were anionic SPIO-based magnetic nanoclusters.

### 2.2. $T_2$ Relaxivity of PAsp-PCL/SPIO Nanocomposites

As MR imaging probes, the $T_2$ relaxivity of PAsp-PCL/SPIO nanocomposites was studied under a clinical 1.5 T MR imaging scanner (Sonata, Siemens). As previously reported,[2c,14] SPIO is an effective $T_2$ contrast agent, which can remarkably speed up spin–spin relaxation, and thus shorten the $T_2$ relaxation time of proton in a given magnetic field. $T_2$ relaxivity, which is

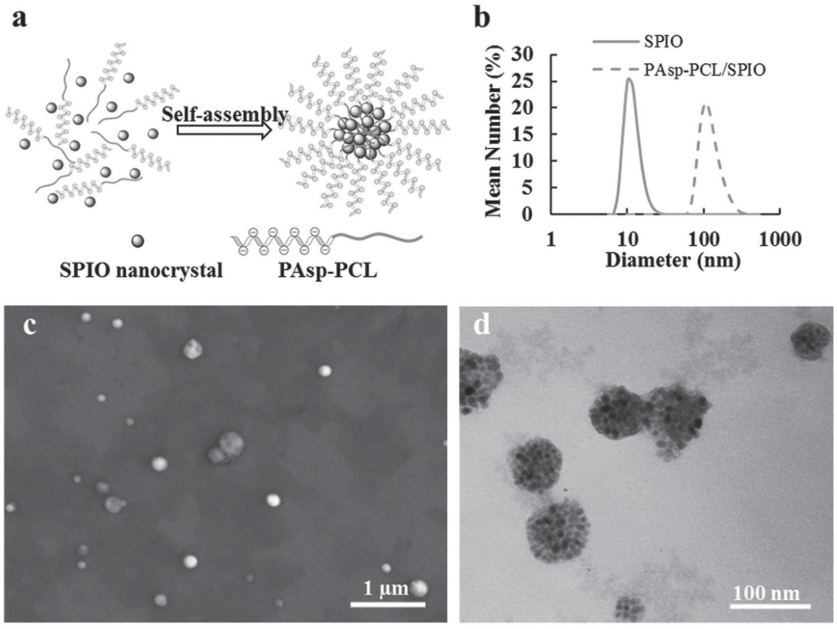


**Figure 2.** a) Schematic illustration of PAsp-PCL/SPIO nanocomposites formation; b) DLS of SPIO nanocrystal in hexane and PAsp-PCL/SPIO nanocomposites in water. Mean diameter of PAsp-PCL/SPIO was 123.9 ± 41.0 nm; c) SEM and d) TEM images of PAsp-PCL/SPIO nanocomposites. The nanocomposites appeared spherical SPIO clusters.

commonly marked as $r_2$, represents the reciprocal of $T_2$ relaxation time per unit concentration of iron element.[15] Previous studies have shown that nanocomposites containing multiple SPIO nanocrystals manifested higher $T_2$ relaxivities than those containing single SPIO nanocrystal,[14b,16] and were even able to distort magnetic field if suspended in a larger volume of solvent. A probable explanation is that nanocomposites hold an increased magnetic moment in an aqueous solution. Herein, a higher $T_2$ relaxivity of the PAsp-PCL/SPIO nanocomposite (335.6 Fe $mM^{-1}$ $s^{-1}$) was observed at 1.5 T magnetic field (**Figure 3**), similar to some previous reports.[2c,17] This imaging property is quite beneficial for it acting either as an MR imaging contrast agent or as a cell-labeling probe.

To investigate the detectable limit of PAsp-PCL/SPIO nanocomposites for MR imaging, we defined the detecting sensitivity as the nanocomposite concentration where MR signal intensity (SI) decreased to 50% of that of pure water on a given $T_2$-weighted image.[17] With regard to PAsp-PCL/SPIO nanocomposites, the measured detection limits were 0.1, 0.06, and 0.03 mM Fe at different echo times (TEs) of 30, 50, and 85 ms (1.5 T, spin-echo sequence, repetition time (TR) = 5 s), respectively. Obviously, enough long TE would result in sensitivity high enough to trace out a few micromolar concentrations of iron. Thus, we believe that PAsp-PCL/SPIO nanocomposite could be utilized as sensitive probes to reveal the minor pathological changes at the molecular or cellular level on MR imaging.

### 2.3. In Vitro Study of Probe Labeling Effects on the Expression of DC Biomarkers

PAsp and PCL are widely used biopolymers with acceptable biocompatibility in many applications. Cytotoxicity of PAsp-PCL/SPIO nanocomposites was tested on two different cell lines (RAW 264.7 and murine DC). The viability and surface phenotyping of cells were examined by DNA fluorometric assay and fluorescence activated cell sorter (FACS).

After being incubated with PAsp-PCL/SPIO nanocomposites for 24 h, cells were collected for visual inspection under a microscope. No observable abnormality was noted of their morphological appearance. DNA fluorometric assay disclosed that both kinds of cells kept similar survival compared to unlabeled control ones when labeled at a probe concentration not exceeding 10 μg Fe $mL^{-1}$. Furthermore, when iron concentration was up to 40 μg Fe $mL^{-1}$, all cells still survived at a rate more than 90%, though the rate of RAW 264.7 was slightly higher than DC. The results suggested that labeling cells with this probe, especially at a concentration within 10 μg Fe $mL^{-1}$, was fairly safe.

To further understand effects of the probe on DCs phenotype, immature DCs, mature unlabeled, and labeled DCs were

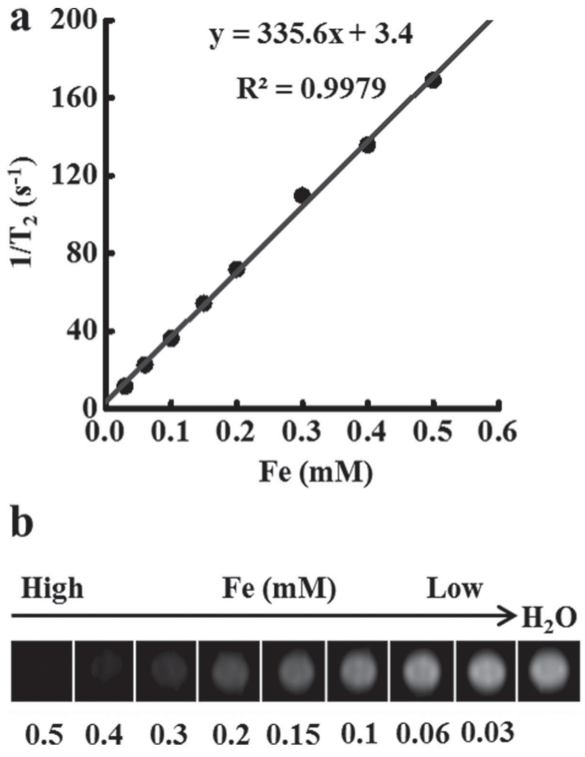


**Figure 3.** a) $T_2$ relaxation rate ($1/T_2$, $s^{-1}$) as a function of Fe concentration (mM) for PAsp-PCL/SPIO nanocomposites at 1.5 T. The slope of curve is $T_2$ relaxivity of PAsp-PCL/SPIO (335.6 Fe $mM^{-1}$ $s^{-1}$); b) $T_2$-weighted MRI images of PAsp-PCL/SPIO nanocomposites in water (1.5 T, spin-echo sequence: TR = 5000 ms, TE = 20 ms, slice thickness = 3 mm, flip angle 90°).

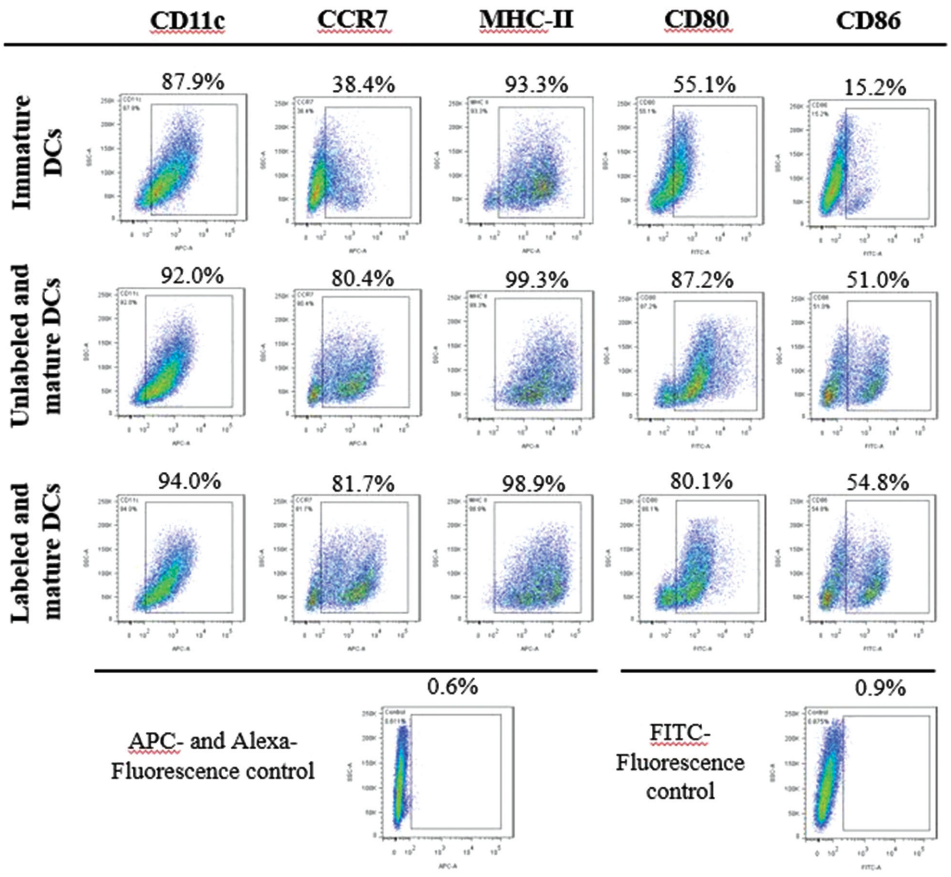


**Figure 4.** Labeling impacts on phenotype of DCs. Expression of CD11c was studied to confirm the purity of DC. The chemokine receptor CCR7, antigen-presenting molecules MHC-II, and costimulatory molecules (CD80 and CD86) were all expressed in a similar level between the unlabeled and labeled mature DCs, and higher compared to immature DCs.

simultaneously analyzed by fluorescence-activated cell sorting (FACS) (**Figure 4**). Expression of CD11c was all close to 90%, confirming that the purity of DCs was comparatively high. Other four major surface markers relevant to DCs maturation were also investigated, including the chemokine receptor CCR7, antigen-presenting molecules MHC class II (MHC-II), costimulatory molecules CD80 and CD86. Resultantly, these markers were all expressed in a similar level between the unlabeled and labeled mature DCs, and both presented obviously increased expression compared to the immature DCs. So, labeling DCs with PAsp-PCL/SPIO nanocomposites would bring little interference to DCs.

### 2.4. Labeling and MR Imaging of DCs In Vitro

#### *2.4.1. Cellular Uptake of PAsp-PCL/SPIO Nanocomposites*

High $T_2$ relaxivity and labeling efficiency of a probe do benefit for the imaging of cells. Factors that influence a probe's $T_2$ relaxivity have already been discussed in Section 2.2. Labeling efficiency of a probe involves its physicochemical properties, cellular uptake ability, probe concentration, and time period for labeling.[2c,18] For example, cationic nanoparticles tend to be taken up by cells than neutral or anionic ones.[5a,8] But when labeling phagocytes, the situation would be different. Phagocytes, such as macrophage and DC, are able to actively capture antigens or other foreign bodies. Taking advantage of this function, one may also attain a desirable labeling effect even with neutral or anionic nanoparticles and at a relatively low concentration. Herein, we labeled DCs with negatively charged nanoprobe, PAsp-PCL/SPIO nanocomposites. The labeling efficiency was investigated by measuring intracellular iron content. Similar to other anionic nanoprobes,[14c] PAsp-PCL/SPIO displayed a time- and dose-dependent labeling pattern (**Figure 5**a). For example, intracellular iron content of DCs would correspondingly increase from 1.0 to 3.5 pg/cell when the incubation period extended from 6 to 24 h at a probe concentration of 10 μg Fe $mL^{-1}$. Though the intracellular iron content was inferior to those commonly used cationic transfect agents,[2c,19] MR imaging sensitivity of labeled DCs was preferable (subsequent results will clarify). TEM and Prussian blue staining followed on to visually evaluate the labeling efficiency. TEM revealed that clusters of dense deposit were found in cytoplasm and confined in certain compartments, indicating the active endocytosis by DCs. In contrast, similar deposits did not exist in the unlabeled DCs, as well as in nuclei of the labeled

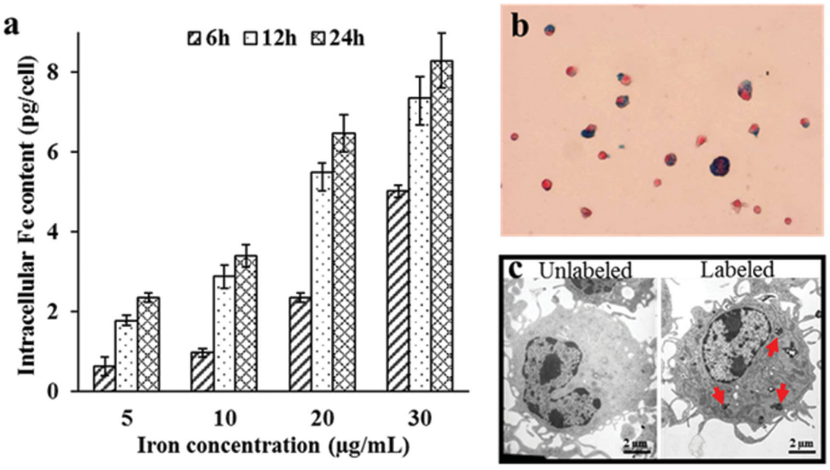


**Figure 5.** a) Intracellular iron content of DCs after labeled with PAsp-PCL/SPIO nanocomposites. The iron uptake process in DCs displays a time- and dose-dependent behavior; b) Prussian blue staining of SPIO-labeled DCs, magnification: 200×; c) TEM of SPIO-labeled and unlabeled DCs (10 μg Fe $mL^{-1}$, 24 h). The high electron density iron oxide particles were marked by red arrows.

DCs (Figure 5c). Pseudopodia of the DCs were also observed, and no difference in morphology was discovered between the labeled and unlabeled DCs. Prussian blue staining showed numerous blue-stained iron particles locating in the cytoplasm. So, PAsp-PCL/SPIO displayed excellent labeling efficiency for DCs.

### 2.4.2. In Vitro MR Imaging of Labeled DCs

MR imaging sensitivity of the labeled DCs was evaluated in vitro under a clinical 3 T MRI scanner. Cells were labeled with the probes at a concentration of 10 mg Fe $mL^{-1}$ for 12 h. Then, the labeled cells were collected and homogenously dispersed in gelatin at graded cell numbers. The prepared phantoms were imaged to detect their MR SI at different TEs. Resultantly, these DCs in the gelatins induced definite reduction of $T_2$-weighted signal intensity, which appeared inversely proportional to the cell number (**Figure 6**a). For example, imaged at TE of 100 ms (TR = 5 s), phantoms that contained $5 \times 10^4$ cells showed an SI approximating to 72% of the control gelatins. Furthermore, when the cell number went up to $1 \times 10^5$, $5 \times 10^5$, or $1.5 \times 10^6$, the ratio declined correspondingly to 58%, 23%, and 19%. $T_2$ values of the phantoms also behaved in a similar mode (Figure 6b), and decreased while the cell number increased. When the cell number was, for an instance, $5 \times 10^5$, $T_2$ value of the phantoms dropped to about 15 ms, only 5% to that of control. These results show that DCs labeled with PAsp-PCL/SPIO nanocomposites have an excellent MR imaging sensitivity.

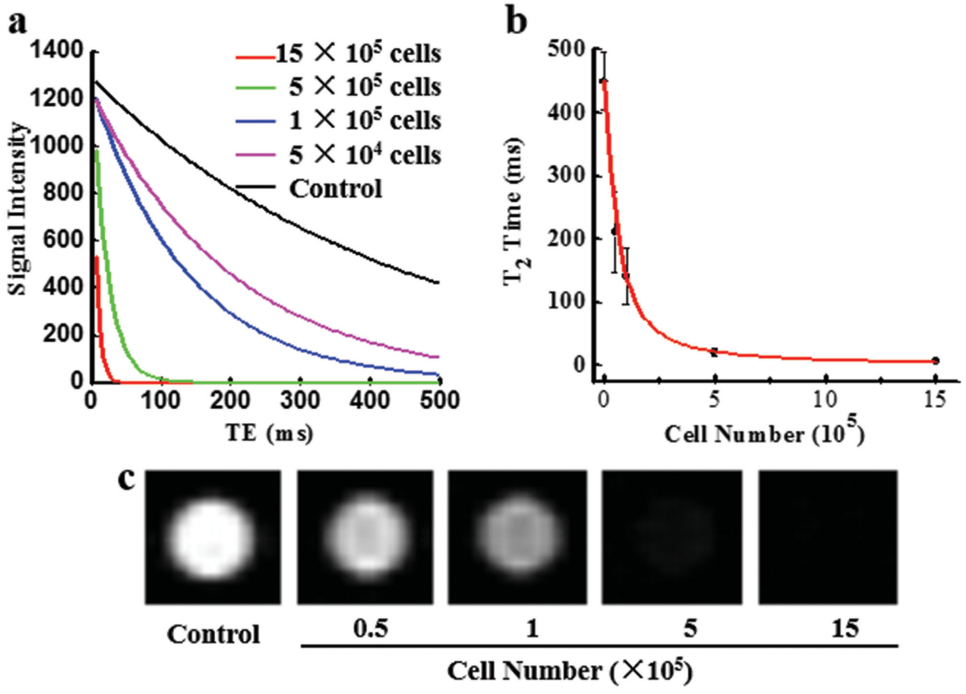


**Figure 6.** a) Plot of curve fitting the SI attenuation on $T_2$-weighted MR image with TE in different cell numbers (ranging from $1.5 \times 10^6$ to $5 \times 10^4$, 3 T, room temperature); b) $T_2$ values of the gelatin phantom, containing PAsp-PCL/SPIO nanocomposite-labeled DCs in microcentrifuge tubes, as a function of cell number; c) Axial MR images of the corresponding tubes under SE acquisition (3 T, spin echo acquisition, TR = 5000 ms, TE = 75 ms).

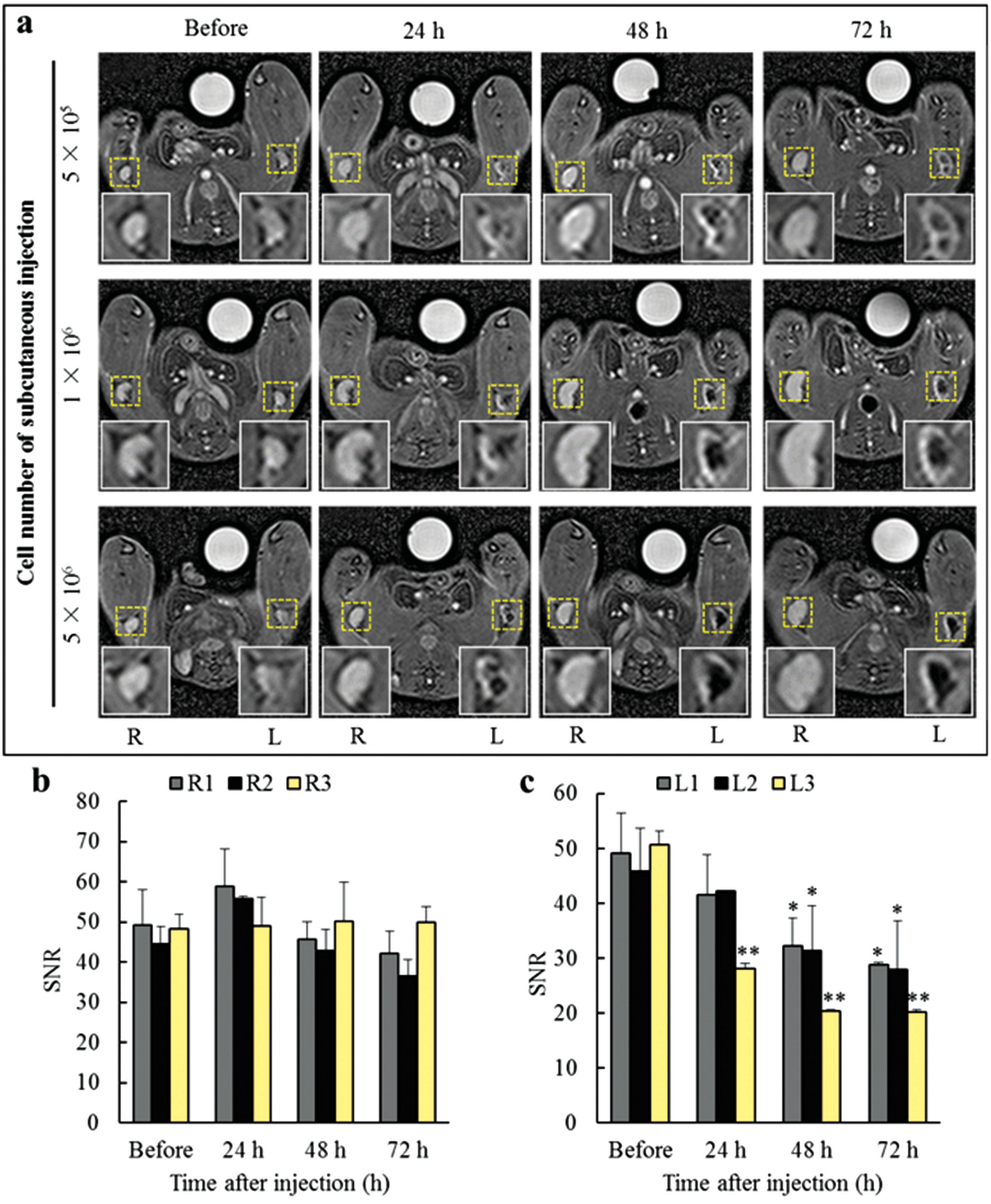


**Figure 7.** $T_2$-weighted TSE images a) of mouse popliteal lymph nodes at different time points before and after hypodermic injection labeled (L, left) and unlabeled (R, right) DCs at the hindleg footpads. The left popliteal lymph nodes showed strong signal intensity reduction, while the right ones showed negligible changes. The results are a representative of three separate experiments. SNR measurements in the b) right and c) left LN at different time points were acquired. Compared with preinjection SNR levels, * = $P < 0.05$, ** = $P < 0.01$ (R1 and L1, $5 \times 10^5$; R2 and L2, $1 \times 10^6$; R3 and L3, $5 \times 10^6$ DCs). TSE sequence: TR = 4000 ms, TE = 64 ms, slice thickness = 1.0 mm, gap = 0.0 mm, matrix = 480 × 480, field of vision = 30 × 30 mm, flip angle = 90°.

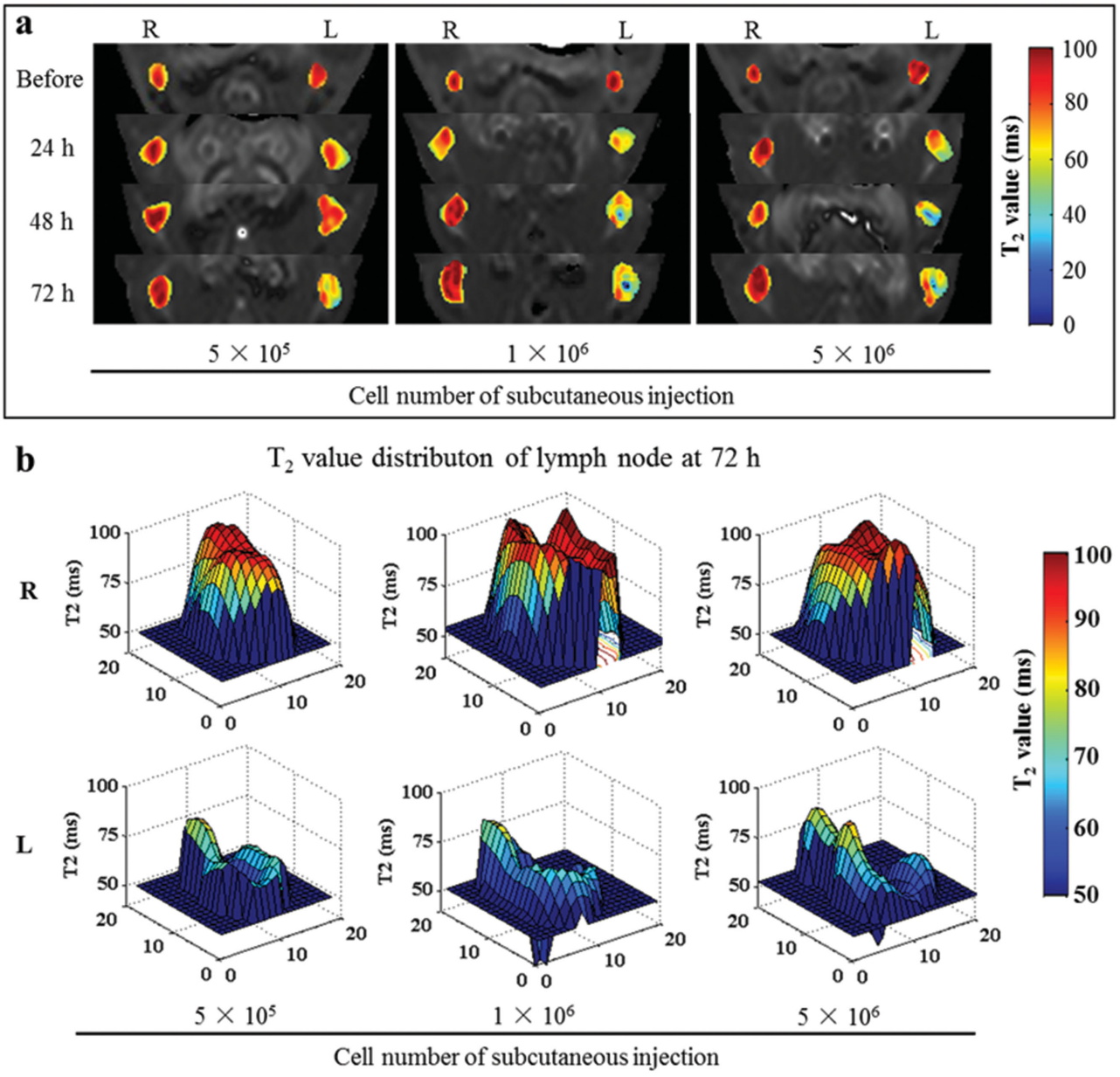


**Figure 8.** $T_2$-map images a) of mouse popliteal lymph node at different time points before and after subcutaneous injection different numbers of labeled (L, left) and unlabeled (R, right) DCs at the hindleg footpads. The left popliteal lymph nodes showed strong $T_2$ shortening, while the right ones showed $T_2$ prolongation in central areas. The effect is more obvious with increasing DCs dose. b) $T_2$ value distributon of lymph node at 72 h after subcutaneous injection acquired. The results are a representative of three separate experiments. $T_2$-map sequence: TSE, TR = 254 ms, TE = 10–100 ms, matrix = 148 × 148, slice thickness = 1.0 mm, gap = 0.0 mm, field of vision = 40 × 40 mm.

### 2.5. In Vivo MRI Tracking of Labeled DCs

#### *2.5.1. Tracking of DCs Migration to the Draining Lymph Nodes by MRI*

To launch immune responses, it is critical that the antigen-laden DCs should successfully migrate to lymphoid organs and present the antigen peptides to T or B cells. Given its importance, imaging technologies have recently been attempted for visually monitoring this process. In this study, we visualized the process via MR imaging. Mice were subcutaneously injected at hind-leg footpads with a certain number of DCs labeled or unlabeled with the nanoprobe, PAsp-PCL/SPIO. For enhancing the homing of DCs, 100 ng TNF-$\alpha$ was beforehand introduced to presensitize the footpads. In the preliminary experiments, after subcutaneous injection with $5 \times 10^6$ labeled DCs at left hind-leg footpads, MR images of popliteal nodes were acquired using $T_2$-wighted turbo spin echo (TSE) and fast field echo (FFE) sequence, respectively (Figure S8, Supporting Information). SI within the central zone of the left nodes all declined with time in two sequences. However, $T_2$-wighted TSE imaging showed a higher tissue resolution and thus was used

in the following experiments. In addition, $T_2$-map imaging was also used to observe the $T_2$ value changes of lymph nodes after injection.

**Figure 7**a shows that the lymph nodes were clearly depicted on cross-section images and all showed gradual enlargement with time on $T_2$-wighted TSE imaging after subcutaneous injection with different numbers of DCs. However, the left and right hind-leg lymph nodes (LNs) presented a different variation in SI. SI within the central zone of the left hind-leg LNs (administration SPIO-labeled DCs at footpads) declined with time, whereas the right hind-leg ones (administration unlabeled DCs at footpads) did not. Mean signal-to-noise ratios (SNR) of LNs under different DCs dosages at different points in time were measured, respectively, and shown in Figure 7b,c. SNR changes of right LNs presented no significant differences, while that of left LNs were obvious, and depended on time and DCs dosages. In a relatively low DCs dose ($5 \times 10^5$), significant difference of left LNs occurred in the following 48 h after administration, and further expanded with time. This change occurred at 24 h in advance with dose of $5 \times 10^6$ DCs. Results showed that SPIO-labeled DCs in footpads were slowly moving to adjacent LN and aroused its SI changes in $T_2$-wighted imaging. Progressive enlargement of LNs represents the proliferation of lymphocytes, a process probably initiated by the immigrated DCs. $T_2$-map studies further revealed that the shortening $T_2$ values of the left LNs appeared dose- and time-dependent, while the right LNs show a $T_2$ values increasing (**Figures 8** and **9**). The increase of $T_2$ values in LNs area is, to our best knowledge, not reported in the DC-related literature. This can be interpreted by the accompanying change in water and protein levels at the local microenvironment.

SI reducing and $T_2$ values shortening of the left nodes may be explained either by the inflow of the naked probes or by the intracellular ones. Inflowing probes usually located at the peripheral zone of LN, resulting in SI reduction at this area. DCs, however, can enter in the deeper regions (the central T cell areas of LN) with the help of CCR7.[20] In this study, the darkened signal and low $T_2$ values were primarily center-located (Figures 7 and 8), which accorded with previous reports, highly suggesting that the changes were due to the active homing of SPIO-laden DCs. This deduction was further confirmed by the subsequent pathological findings.

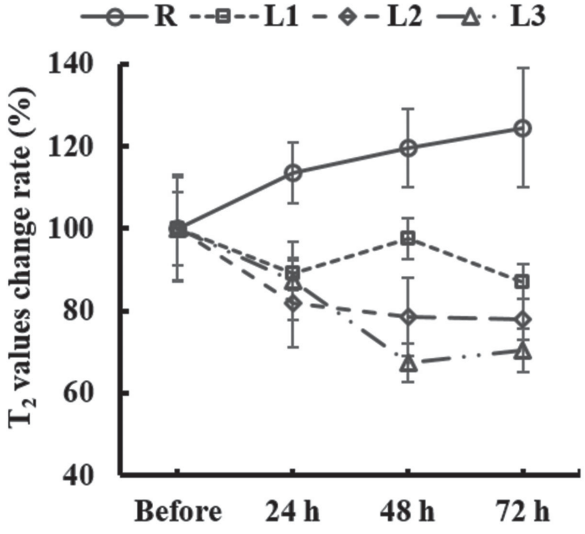


**Figure 9.** $T_2$ value change rate of mouse popliteal lymph node at different time points before and after subcutaneous injection of different numbers of DCs at the hindleg footpads. $T_2$ values of right (R) lymph node increased over time, while that of left (L1, L2, and L3) lymph node gradually decreased. (R, unlabeled DCs; L1, $5 \times 10^5$ labeled DCs; L2, $1 \times 10^6$ labeled DCs; L3, $5 \times 10^6$ labeled DCs).

Our findings have disclosed a dose-dependent relationship between injected cells and homing cells, but we do not feel it is necessary to inject too many DCs at footpads. Theoretically, it seems that the more cells are injected, the more cells would arrive at lymph nodes. In fact, DCs' homing is always under the effect of a series of complicated factors. Biological state of cells, probes' interference on cell function, preparation of local lymphatic system, and the number of the injected cells, etc., all bring impacts upon their migration motion. Too many cells injected at a site would cause locally deficit of oxygen and nutrition, or blockage of the afferent lymphatic vessels, thus impairing their homing. Moreover, overload of probes in cytoplasm would damage the flexibility of DCs, weakening their immigration ability. Therefore, it seems more reasonable to label DCs with small amounts of probe and inject in a multiple and small-dose mode, as proposed by recent literature.[21]

#### *2.5.2. Pathological Study of Lymph Nodes*

Immediately after the MR imaging at 72 h, the bilateral popliteal nodes of mice were extracted for pathological exams. Serial sections were offered sequentially for hematoxylin and eosin (HE) staining, Prussian blue staining, and CD3 immunostaining. Prussian blue staining showed that blue iron particles located intracellularly and were found in all the left-side nodes, while none in the right-side ones (administration SPIO-labeled DCs at left-side footpads and unlabeled DCs at right-side footpads). A significant difference existed between any two groups with the same cell number. A comparation of HE and CD3 staining revealed that vast mojortity of the cells located within the T cell zone of LN, corresponding to the central distribution viewed on MR images (panels c–f in **Figure 10**). Moreover, the averaged number of the iron-containing cells in prussian blue staining strongly correlated ($R^2 = 0.9898$) with the $T_2$ values of lymph nodes (**Figure 11**), suggesting that the labeled DCs perhaps were the contributors of SI reduction. Together, we believe that the iron-containing cells in the T cell zone of lymph nodes represent the active immigration of the labeled DCs that were originally injected at foodpads. The migration is a key step in the DC-based immunotherapy, an essential condition of inducing the immune response depends on T cell activation, and can be monitored by safe and noninvasive MR imaging.

## 3. Conclusion

This study has rendered polypeptide–polyester based negatively charged MR imaging probes, PAsp-PCL/SPIO nanocomposites, showing excellent $T_2$ relaxivity (335.6 Fe $mM^{-1}$ $s^{-1}$). The

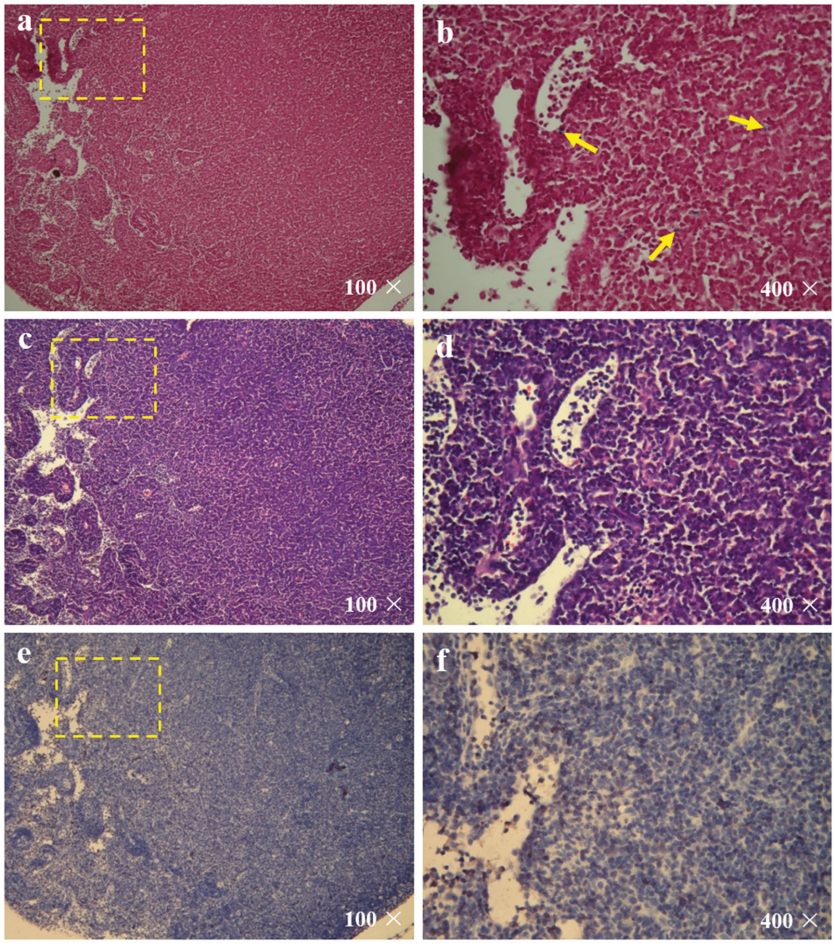


**Figure 10.** a,b) Prussian blue staining, c,d) H&E staining, and e,f) CD3 immunostaining of the left-side popliteal lymph node at 72 h. A mouse was subcutaneously injected $1 \times 10^6$ labeled DCs at the footpad. Magnification 100× for images of ace, 400× for bdf.

probes can easily be taken up by DCs without significant effects on their surface key biomarker expressions. DCs labeled with these probes can remarkably shorten the $T_2$ values, and can clearly be observed migrating to their draining lymph nodes, upon injection at footpads of mice. In summary, PAsp-PCL/SPIO nanocomposites, as a safe and effective probe, can be utilized for the labeling and tracking of cell vaccines such as DCs.

## 4. Experimental Section

*Preparation and Characterization of PAsp-PCL/SPIO Nanocomposites*: Details on synthesis and characterization of PAsp-PCL block copolymer were provided in the Supporting Information. Briefly, organic SPIO nanocrystals were synthesized via the high-temperature decomposition method, and transferred to the water phase with PAsp-PCL to obtain self-assembled PAsp-PCL/SPIO nanocomposites. Size distribution and morphology of PAsp-PCL/SPIO nanocomposites were characterized by DLS, SEM, and TEM, respectively. $T_2$ relaxivities were measured, as previously described, under a clinical 1.5 T Siemens MR scanner at room temperature.[16]

*Cytotoxicity and DC's Labeling Efficiency Assays*: Cytotoxicity of the probe PAsp-PCL/SPIO nanocomposites was studied with DNA assay and FACS. Cytotoxicity was tested with two different cell lines (Raw 264.7 and DC). Specifically, cells were inoculated in 48-well plates at $2 \times 10^5$ cells/500 µL per well, and coincubated with PAsp-PCL/SPIO nanocomposites of graded concentrations (5, 10, 20, and 40 µg mL$^{-1}$) at 37 °C in a humidified incubator containing 5% $CO_2$. Twenty-four hours later, cells were harvested and washed with PBS. Deionized water (250 µL) was added to each well. Then, the cells went through a freeze-and-thaw cycle for lysis. In a dark place, 500 µL Hoechst 33258 work solution (0.75 µg mL$^{-1}$, Sigma-Aldrich) was added to incubate for 2 h. Finally, the sample plates were read at 460 nm using a plate reader. A relationship between cell viability and absorbance was hence established according to the following equation: cell viability (%) = (Ni/Nc) × 100, where Ni and Nc are the absorbance of cells treated with or without PAsp-PCL/SPIO nanocomposites, respectively. For further understanding the biological safety of PAsp-PCL/SPIO nanocomposites, DCs were labeled and submitted for FACS assays to find their impacts on DC maturation. Four major surface markers relevant to DC maturation were investigated, including CCR7, MHC-II, CD80, and CD86. To carry out the tests, $2 \times 10^6$ mature-and-labeled DCs per sample, with both immature and mature-and-unlabeled DCs as control, were suspended in 50 µL PBS, and incubated with 2 µL monoclonal antibodies for 30 min. After being washed with PBS, the samples were examined by a flow cytometer (FACSAria, BD). Antibodies used for the assay were all purchased from the BD Biosciences. They were allophycocyanin (APC)-conjugated anti-CD11c (HL3), Alexa Fluor-conjugated MHC class II (M5/114.15.2), fluorescein isothiocyanate (FITC)-conjugated anti-CD80 (16-10A1), FITC-conjugated anti-CD86 (GL1), and Alexa Fluor-conjugated anti-CCR7 (CD197, 4B12). Unstained DC samples were recruited to subtract the

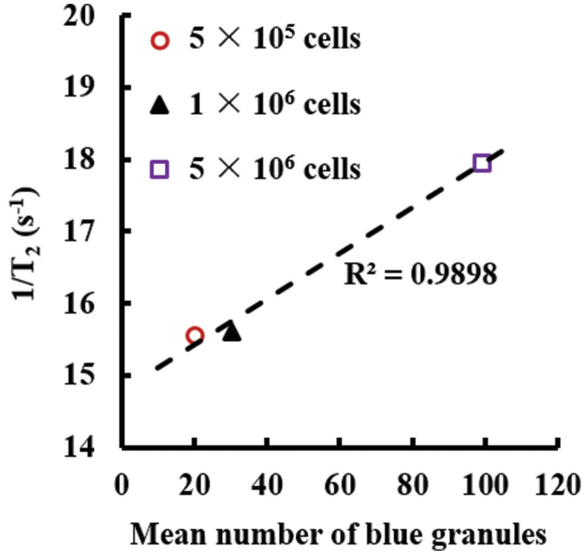


**Figure 11.** Graph illustrates relationship between relaxation rate ($1/T_2$) of LN at 72 h and mean blue granules number in Prussian blue staining of LNs ($R^2 = 0.9898$; simple linear-regression analysis) after hypodermic injection $5 \times 10^6$, $1 \times 10^6$, and $5 \times 10^5$ labeled DCs at the footpad.

background fluorescence. Cellular labeling efficiency was analyzed by measurement of intracellular iron content, TEM, and Prussian blue staining. To quantify the intracellular iron, DCs were seeded, at $2 \times 10^5$ cells $mL^{-1}$ per well, into 48-well plates, and incubated with different concentrations of PAsp-PCL/SPIO nanocomposites (equivalent of 5, 10, 20, and 30 μg Fe $mL^{-1}$) for different incubation periods (6, 12, and 24 h). At the end of each time point, cells were harvested with three washes. Iron-releasing reagent (mixture of equal volume of 1.4 M HCl and 4.5% (w/v) $KMnO_4$ in $H_2O$) was added and incubated for 2 h at 60 °C within a drying oven. When cooled to room temperature, iron detection reagent ($6.5 \times 10^{-3}$ M ferrozine, $6.5 \times 10^{-3}$ M neocuproine, 2.5 M ammonium acetate, and 1 M ascorbic acid dissolved in water) was applied. Thirty minutes later, the plates were read at 570 nm with a microplate reader. Iron contents were determined by comparing their absorbance to the standard solutions. Prussian blue staining was employed to visually display the nanocomposites within the labeled DCs. In brief, cells were washed and resuspended in FBS-containing PBS. A few drops of the suspension were smeared upon a slide. The slides were then incubated with Prussian blue reagent for 30 min, and counterstained of cellular nuclei with Nuclear Fast Red. The stained slices were studied under a light microscope. TEM was applied to further observe the ultrastructure of the labeled DC. To this aim, cells were washed and centrifuged (10 000 rpm, 15 min). Three percent of glutaraldehyde in $50 \times 10^{-3}$ M cacodylate buffer was added to fix the resulted pellets. After 15 min, pellets were washed with PBS and incubated in 1% osmium tetroxide for 2 h, followed by dehydrating through graded alcohols and embedding in epoxy resin. Ultrathin sections were cut, stained with 1% uranyl acetate and lead citrate, and then photographed under an H600-IV transmission electron microscope (Hitachi, Japan).

*In Vitro MRI Study of the Labeled DCs*: DCs were labeled with the probes at a concentration of 10 mg Fe $mL^{-1}$. Twelve hours later, cells were collected and divided into four groups ($n = 5$) in different numbers, i.e., $1.5 \times 10^6$, $5 \times 10^5$, $1 \times 10^5$, and $5 \times 10^4$. Then, cells were mixed with 200 μL 5% gelatin crosslinked with glutaraldehyde inside microcentrifuge tubes. Gelatin phantoms without cells were recruited as control. MR imaging was performed under a clinical 3 T scanner and with a head coil. Axial images of the phantoms were acquired by $T_2$-weighted spin echo sequence (TR = 5000 ms, TE = 6.9–500 ms; number of averages, 1, matrix = 384 × 224, field of vision = 250 × 190 mm, slice thickness = 2.0 mm). SIs at different TE were measured to calculate the $T_2$ value of each phantom.

*In Vivo MRI Tracking of DCs*: The detailed procedures were described in Supporting Information. Briefly, DCs were incubated with the probes, and stimulated to maturation by the addition of LPS and TNF-$\alpha$. Nine BALB/c mice were randomly assigned into three groups ($n = 3$). Mice in different groups were injected with SPIO-labeled DCs at the left hindleg footpads, and unlabeled DCs at the right hindleg footpads. The injected cell number was $5 \times 10^6$, $1 \times 10^6$, and $5 \times 10^5$, respectively. At 24, 48, and 72 h after the injection, MR imaging was performed on a clinical 3 T scanner. Echo signals of the popliteal lymph nodes were acquired along the *Z*-axis with a $T_2$-wighted TSE sequence and a $T_2$-map sequence.

## Supporting Information

Supporting Information is available from the Wiley Online Library or from the author.

## Acknowledgements

C.W. and Y.X. contributed equally to this work. The work was supported by National Key Basic Research Program of China (2013CB933903), National Key Technology R&D Program (2012BAI23B08), National Natural Science Foundation of China (20974065, 51173117, and 50830107), and Program for Changjiang Scholars and Innovative Research Team in University (PCSIRT, Grant No. IRT1272) of China.

Received: March 16, 2015
Revised: April 13, 2015
Published online: May 7, 2015

[1] a) J. W. M. Bulte, *Am. J. Roentgenol.* **2009**, *193*, 314; b) J. W. M. Bulte, D. L. Kraitchman, *Curr. Pharm. Biotechnol.* **2004**, *5*, 567; c) D. Kim, K. S. Hong, J. Song, *Mol. Cells* **2007**, *23*, 132; d) D. L. Kraitchman, A. W. Heldman, E. Atalar, L. C. Amado, B. J. Martin, M. F. Pittenger, J. M. Hare, J. W. M. Bulte, *Circulation* **2003**, *107*, 2290; e) W. Liu, J. A. Frank, *Eur. J. Radiol.* **2009**, *70*, 258; f) A. S. Arbab, W. Liu, J. A. Frank, *Expert Rev. Med. Devices* **2006**, *3*, 427; g) M. Srinivas, A. Heerschap, E. T. Ahrens, C. G. Figdor, I. J. M. de Vries, *Trends Biotechnol.* **2010**, *28*, 363.

[2] a) E. Amstad, M. Textor, E. Reimhult, *Nanoscale* **2011**, *3*, 2819; b) A. Bhirde, J. Xie, M. Swierczewska, X. Y. Chen, *Nanoscale* **2011**, *3*, 142; c) G. Liu, Z. Wang, J. Lu, C. Xia, F. Gao, Q. Gong, B. Song, X. Zhao, X. Shuai, X. Chen, H. Ai, Z. Gu, *Biomaterials* **2011**, *32*, 528.

[3] C. Tassa, S. Y. Shaw, R. Weissleder, *Acc. Chem. Res.* **2011**, *44*, 842.

[4] a) C. Wilhelm, F. Gazeau, *Biomaterials* **2008**, *29*, 3161; b) S. J. Dodd, M. Williams, J. P. Suhan, D. S. Williams, A. P. Koretsky, C. Ho, *Biophys. J.* **1999**, *76*, 103; c) R. Weissleder, H. C. Cheng, A. Bogdanova, A. Bogdanov, *J. Magn. Reson. Imaging* **1997**, *7*, 258; d) T. C. Yeh, W. Zhang, S. T. Ildstad, C. Ho, *Magn. Reson. Med.* **1993**, *30*, 617.

[5] a) D. L. J. Thorek, A. Tsourkas, *Biomaterials* **2008**, *29*, 3583; b) A. S. Arbab, L. A. Bashaw, B. R. Miller, E. K. Jordan, B. K. Lewis, H. Kalish, J. A. Frank, *Radiology* **2003**, *229*, 838.

[6] W. Zhiyong, L. Gang, S. Jiayu, W. Bing, G. Qiyong, S. Bin, A. Hua, G. Zhongwei, *J. Nanosci. Nanotechnol.* **2009**, *9*, 378.

[7] A. S. Arbab, G. T. Yocum, L. B. Wilson, A. Parwana, E. K. Jordan, H. Kalish, J. A. Frank, *Mol. Imaging* **2004**, *3*, 24.

[8] K. Montet-Abou, X. Montet, R. Weissleder, L. Josephson, *Mol. Imaging* **2007**, *6*, 1.

[9] a) C. Wilhelm, C. Billotey, J. Roger, J. N. Pons, J. C. Bacri, F. Gazeau, *Biomaterials* **2003**, *24*, 1001; b) C. Wilhelm, F. Gazeau, J. Roger, J. N. Pons, J. C. Bacri, *Langmuir* **2002**, *18*, 8148.

[10] Z. Cheng, A. Al Zaki, J. Z. Hui, V. R. Muzykantov, A. Tsourkas, *Science* **2012**, *338*, 903.

[11] a) L. Matera, *Cancer Treat. Rev.* **2010**, *36*, 131; b) L. Engell-Noerregaard, T. H. Hansen, M. H. Andersen, P. T. Straten, I. M. Svane, *Cancer Immunol. Immunother.* **2009**, *58*, 1; c) A. A. Chiappori, H. Soliman, W. E. Janssen, S. J. Antonia, D. I. Gabrilovich, *Expert Opin. Biol. Ther.* **2010**, *10*, 983.

[12] H. Arimura, Y. Ohya, T. Ouchi, *Macromol. Rapid Commun.* **2004**, *25*, 743.

[13] S. Sun, H. Zeng, D. B. Robinson, S. Raoux, P. M. Rice, S. X. Wang, G. Li, *J. Am. Chem. Soc.* **2003**, *126*, 273.

[14] a) J. Xie, G. Liu, H. S. Eden, H. Ai, X. Chen, *Acc. Chem. Res.* **2011**, *44*, 883; b) H. Su, Y. Liu, D. Wang, C. Wu, C. Xia, Q. Gong, B. Song, H. Ai, *Biomaterials* **2013**, *34*, 1193; c) G. Liu, J. Xie, F. Zhang, Z. Wang, K. Luo, L. Zhu, Q. Quan, G. Niu, S. Lee, H. Ai, X. Chen, *Small* **2011**, *7*, 2742.

[15] H. Ai, C. Flask, B. Weinberg, X. T. Shuai, M. D. Pagel, D. Farrell, J. Duerk, J. Gao, *Adv. Mater.* **2005**, *17*, 1949.

[16] Z. Wang, G. Liu, J. Sun, B. Wu, Q. Gong, B. Song, H. Ai, Z. Gu, *J. Nanosci. Nanotechnol.* **2009**, *9*, 378.

[17] J. Lu, S. Ma, J. Sun, C. Xia, C. Liu, Z. Wang, X. Zhao, F. Gao, Q. Gong, B. Song, X. Shuai, H. Ai, Z. Gu, *Biomaterials* **2009**, *30*, 2919.

[18] a) D. Fayol, N. Luciani, L. Lartigue, F. Gazeau, C. Wilhelm, *Adv. Healthcare Mater.* **2013**, *2*, 313; b) M. Safi, M. H. Yan, M. A. Guedeau-Boudeville, H. Conjeaud, V. Garnier-Thibaud, N. Boggetto, A. Baeza-Squiban, F. Niedergang, D. Averbeck, J. F. Berret, *ACS Nano* **2011**, *5*, 5354.

[19] A. S. Arbab, G. T. Yocum, H. Kalish, E. K. Jordan, S. A. Anderson, A. Y. Khakoo, E. J. Read, J. A. Frank, *Blood* **2004**, *104*, 1217.

[20] D. Baumjohann, A. Hess, L. Budinsky, K. Brune, G. Schuler, M. B. Lutz, *Eur. J. Immunol.* **2006**, *36*, 2544.

[21] a) G. A. Dekaban, A. M. Hamilton, C. A. Fink, B. Au, S. N. de Chickera, E. J. Ribot, P. J. Foster, *Wiley Interdiscip. Rev. Nanomed. Nanobiotechnol.* **2013**, *5*, 469; b) H. Hon, J. Jacob, *Immunol. Res.* **2004**, *29*, 69.